Formation of nanocrystalline grain structure in an Mg-Gd-Y-Zr alloy processed by high-pressure torsion

Xinyu Ren[a], Xinglong An[a], Song Ni[a,*], Yi Huang[b,c], Min Song[a]

a - State Key Laboratory of Powder Metallurgy, Central South University, Changsha 410083, China

b - Department of Design and Engineering, Faculty of Science and Technology, Bournemouth University, Poole, Dorset BH12 5BB, UK

c - Materials Research Group, Department of Mechanical Engineering, University of Southampton, Southampton SO17 1BJ, UK

Abstract

In this paper, the microstructural and hardness evolutions of an Mg-5.91Gd-3.29Y-0.54Zr (wt.%) alloy during high-pressure torsion (HPT) were investigated. Deformation twinning played a crucial role in the HPT-induced grain subdivision process. In the 1/8-revolution disk, $\{10\bar{1}1\}$ and $\{10\bar{1}2\}$ twins with different twin variants, $\{10\bar{1}1\} - \{10\bar{1}2\}$ secondary twins and twin-twin interactions were activated. Primary twins prevailed at the very central region of the disk, while much finer multiple twins were formed at the edge region of the disk corresponding to the area subjected to a relatively large plastic strain. Besides, dislocation cell substructures were also developed. Nanocrystalline structure was attained after 5-revolution HPT processing, and the maximum hardness reached ~120 Hv at the edge region of the disk, which is much higher than that achieved from other traditional plastic deformation methods.

Keywords: Mg-Gd-Y-Zr alloy; high-pressure torsion; grain refinement; deformation twinning

---

*Corresponding author, email: song.ni@csu.edu.cn

1. Introduction

Magnesium (Mg) alloys, reputed as a kind of green structural materials in 21st century, have a wonderful application prospects in the fields like aerospace, automotive and military industries due to the low density, high specific strength and stiffness, excellent damping performance and electromagnetic shielding performance [1, 2]. However, the low absolute strength, poor plasticity at room temperature and poor heat resistance of Mg alloys have hindered the practical application [3, 4]. Alloying is an important way to improve the properties of Mg alloys, and Mg-Gd-Y-Zr alloy is one of the most successful examples with high-performance alloy development. The addition of rare earth (RE) elements such as Gd and Y promotes the formation of precipitates with high melting point, and thus the alloys can be strengthened by solution strengthening and aging strengthening. The presence of RE elements can also activate the non-basal slip, weaken the texture and improve the plasticity [5-7]. However, the yield strength of the cast Mg-Gd-Y-Zr alloy can only reach ~150 MPa, and further strengthening is required.

Among all strengthening methods, grain refinement strengthening is an effective method that can improve the strength and ductility simultaneously for Mg alloys [8-10]. According to the Hall-Petch effect, the strength will increase with the decrease of grain size. Meanwhile, fine grains shorten the dislocation slip distance and result in a more uniform deformation. Kang et al. [11] investigated the grain size effect on tensile properties of pure Mg and found that the refinement of Mg grains can not only improve the strength but also the ductility due to the activation of more non-basal dislocations, which is helpful to accommodate strain along c-axis. Therefore, the grain refinement of Mg alloys has always been the research focus. In previous studies, grain refinement was mainly carried out by traditional deformation technologies such as forging [12, 13],

extrusion [2, 14], and rolling [15, 16]. However, these deformation processes have limited effect on grain refinement. And the generation of strong texture that leads to harmful anisotropic mechanical properties cannot be avoided. High-pressure torsion (HPT) has been proved to be an effective method to refine grains to sub-micron scale or even nano scale, and improve the mechanical properties drastically [17, 18]. In this process, the material is not only compressed by the high pressure between the anvils, but also subjected to shear deformation caused by the rotation of one of the anvils [17, 18]. With the grain size being refined to sub-micron or even nano range, the low-temperature forming and high strain hardening of Mg alloys can be realized at the same time [19]. It is reported that the ultimate tensile strength (UTS) and yield strength (YS) of an Mg-Y-Gd-Zr alloy can reach 475 MPa and 450 MPa respectively after HPT processing for 10 revolutions at 200 ºC [20]. Sun et al. [21] investigated the age-hardening behavior of an Mg-8.2Gd-3.8Y-1.0Zn-0.4Zr (wt.%) alloy prepared by HPT and found that after ageing for 12h at 120 ºC, the crystallite size could be refined to ~45.4 nm, reaching a hardness of ~126 Hv. The deformation behavior of pure Mg processed by HPT has also been studied and it turned out that grain boundary sliding played an important role in the improvement of ductility [22]. Although much attention has been paid to the grain refinement strengthening in the research of magnesium alloys, there are still no unified conclusions on the deformation mechanism during HPT processing. In order to further regulate and understand the structural evolution during HPT deformation, the specific process of grain refinement is worthy of in-depth study.

In this study, an Mg-5.91Gd-3.29Y-0.54Zr alloy was deformed by HPT at room temperature. The microstructural and hardness evolutions were investigated to explore the grain refinement mechanism as well as the strengthening mechanism induced by HPT. In addition, the function of dislocations and multiple twins in the deformation

process were discussed in detail.

2. Experimental procedures

The as-cast ingot with chemical compositions of Mg-5.91Gd-3.29Y-0.54Zr (wt.%), measured by inductively coupled plasma atomic emission spectroscopy (ICP), was studied in this paper. The ingot was first homogenized at 520 ℃ for 12 h to get supersaturated solid solution (denoted as-SSSS), then machined into disks with a diameter of 10.0 mm and a thickness of 1.0 mm. Before HPT process, the dicks were ground with abrasive papers on both sides to a final thickness of ~0.8 mm. The HPT processing was conducted on a quasi-constrained HPT facility at room temperature under an imposed pressure of 6.0 GPa and at a rotational speed of 1 rpm with 1/8 and 5 revolutions, respectively.

The Vickers microhardness across the diameter of the disks was measured by a BUEHLER 5104 microhardness tester under a load of 500 g for 15 s. The hardness values were averaged from 8 datum points equally far from the center of the disk. After removing the oxide layer, the disk samples were analyzed on a Rigacu corporation Smart Lab 3KW X-ray diffractometer with a scanning angle of 10° to 90°. Samples for the optical microscope (OM) observation on a Leica 4500P OM were mechanically polished and then etched with 4% sodium citrate solution. The scanning electron microscope (SEM), energy dispersive spectrometer (EDS) and electron back-scattering diffraction (EBSD) analysis was conducted by an FEI Helios Nanolab G3 UC scanning electron microscope. Samples for SEM observation were mechanically polished to mirrorlike state. Samples for EBSD observation were prepared by mechanical grinding and then electropolishing in a solution of 2% perchloric acid + 98% ethanol at a voltage of 25 V and a temperature of −35 ° C for 2 minutes. To further identify the

microstructure, samples were examined by transmission electron microscopy (TEM) (Titan G2 60-300). Samples for TEM observation were mechanically ground to 70 μm and then electropolished in a twin-jet machine with an electrolyte of 2% perchloric acid + 98% ethanol at a voltage of 30 V and a temperature of −35 ℃.

3. Results and discussion

Fig. 1 shows the back-scattered SEM images, elemental mappings, and EDS analysis at selected positions of the as-cast and as-SSSS samples. As shown in Fig.1a, obvious contrast difference and discontinuous island phases can be observed at grain boundary areas in the as-cast sample. These areas are rich in Gd and Y and poor in Mg from the elemental mapping analysis in Fig.1b. EDS analysis was taken at positions A, B and C in Fig.1c. The atomic ratio of Mg and (Gd+Y) at position B is close to 24:5, indicating that the island phases correspond to $Mg_{24}(Gd,Y)_5$. In addition, an unknown phase at position C is rich in Gd, Y and Zr. After solution treatment, as shown in Fig.1d, the island phases were almost dissolved in the matrix and only a few cuboid-shaped phases were sparsely distributed in the α-Mg matrix. EDS analysis indicated that these cuboid-shaped phase was rich in Gd, Y and Zr.

Fig. 2a shows the distribution of microhardness of the as-SSSS sample and the HPT-processed samples along the diameter. The average microhardness value of the as-SSSS sample was measured to be ~71 Hv, as indicated by a blue solid line, with the standard deviations marked by blue dashed lines. After HPT processing for 1/8 revolution, the microhardness increases to ~83 Hv at the center position of the disk and ~99 Hv at the edge position. After 5 revolutions, the microhardness increases to ~103 Hv at the center and ~120 Hv at the edge. It is obvious that the microhardness increases with both the radius and the HPT revolutions. The symmetrical distribution of hardness

along the diameter agrees with the distribution of strain on the disk which increases from the center to the edge. Fig. 2b shows the XRD spectra of Mg-5.91Gd-3.29Y-0.54Zr alloy before (as-SSSS) and after HPT processing, and the spectra between 31° and 39° were further magnified and inserted in the upper left corner. Only α-Mg was detected in the as-SSSS sample, indicating that most of the second phase was dissolved in matrix after solid solution treatment. After HPT processing, no additional peaks appear and the peaks for α-Mg broadened as the revolution increases, indicating the refinement of the grain size and the increased internal stress.

The optical microscope images in Fig.3 present the microstructure along the radius of the disk after HPT processing for 1/8 and 5 revolutions. Fig. 3a demonstrates that there is no significant difference in the grain size of the 1/8-revolution sample compared to the as-SSSS sample. The central region and edge region of the disk were further magnified in Fig.3b and 3c to extract more structural details. It can be seen that flat twins were activated in some grains at the central area as indicated by white arrows, while much finer lamellas in multiple directions were formed and intersected in almost all the grains at the edge part of the disk, which might be multiple twins and would be further analyzed by EBSD. From Fig.3d-f, after 5 revolutions, grains can be seen clearly at the very center of the disk, while at the region with r=2-3mm, the grains were severely deformed accompanied with the collapse of grain boundaries. In the periphery region with r=4-5mm, there are no longer continuous grain boundaries, and the detailed microstructure cannot be visualized clearly under optical microscope.

In order to further understand the microstructural evolution, EBSD characterization was conducted on the 1/8-revolution sample. Note that EBSD data of 5-revolution sample cannot be obtained with high quality due to the quite large internal stress. It can be seen from the image quality (IQ) figure of the 1/8-revolution sample, as shown in

Fig.4a, that twins were activated in multiple directions in grains. G1, G2 and G3 represent grains 1, 2 and 3, respectively. Note that G3 is much more refined by high density of multiple twins, and the boundaries in G3 are hard to be determined. Fig. 4b and 4c show the inverse pole figure (IPF) and IQ boundary map of the area containing G1 and G2. Three types of $\{10\bar{1}2\}$ twin variants (T1, T2 and T3 in Fig.4d) were observed in G1, while one $\{10\bar{1}2\}$ twin variant and $30°\{10\bar{1}1\} - \{10\bar{1}2\}$ secondary twins (T1 and ST in Fig.4e) were observed in G2. Figs.4f and 4g show the line profiles of the misorientation angles along arrows AB and CD in Fig.4a. A large number of peaks at around 30° were shown in Fig.4f, which corresponds to the misorientation angle of $30°\{10\bar{1}1\} - \{10\bar{1}2\}$ secondary twin, indicating that many 30° secondary twins may be activated in this region. The presence of numerous peaks in Fig.4g indicates that G3 was divided by a large number of boundaries. Comparing the peak values with the misorientation angles of twins, it is proposed that a lot of $\{10\bar{1}1\}$, $\{10\bar{1}2\}$, and $30°\{10\bar{1}1\} - \{10\bar{1}2\}$ twins may be activated in G3.

Fig.5 shows the EBSD analysis results of another area in the 1/8-revolution HPT sample. $\{10\bar{1}2\}\langle10\bar{1}1\rangle$ tensile twins, $\{10\bar{1}1\}\langle10\bar{1}2\rangle$ compression twins and $\{10\bar{1}1\} - \{10\bar{1}2\}$ secondary twins were observed. It is noticed that $\{10\bar{1}1\} - \{10\bar{1}2\}$ secondary twins are the most common in this grain. To further analyze the formation mechanism of the secondary twin, a rectangular area in Fig. 5b is enlarged in Fig. 5c, with the corresponding pole figure shown in Fig. 5d. Grain A exhibits a misorientation angle of $57°\langle11\bar{2}0\rangle$ with grain B, which obeys the $\{10\bar{1}1\}$ twin relationship, while grain B exhibits a misorientation of $85°\langle11\bar{2}0\rangle$ with C, which agrees with the $\{10\bar{1}2\}$ twin relationship. This finally leads to a $38°\langle11\bar{2}0\rangle$ misorientation between A and C, corresponding to the $\{10\bar{1}1\} - \{10\bar{1}2\}$ secondary twin relationship. Fig. 5e shows the distribution of the misorientation angles in Fig.5c. The inserted inverse pole figures

reflect the rotation axis distributions of the misorientation peaks. Three distinct peaks at around 30°, 38° and 85° further confirms the existence of $30°\{10\bar{1}1\}-\{10\bar{1}2\}$ secondary twin, $38°\{10\bar{1}1\}-\{10\bar{1}2\}$ secondary twin and $85°\{10\bar{1}2\}$ tensile twin, respectively. Note that both $30°\{10\bar{1}1\}-\{10\bar{1}2\}$ and $38°\{10\bar{1}1\}-\{10\bar{1}2\}$ secondary twins were observed in this area, which is due to different twin variant selection. Due to the lack of slip systems, twins play an important role in the deformation of Mg alloys. The initial orientation of an individual grain has great impact on the twinning sequence. The twin variant selection mainly depends on the Schmid law [23]. Besides, a few non-Schmid twins can also be activated along the short axis of the parent grains due to the relatively short twinning free path [23]. Usually, $\{10\bar{1}2\}$ extension twins dominate the twin type in the case of conventional Mg alloys due to its lowest critical resolved shear stress. The $\{10\bar{1}2\}$ twin has a high mobility and is conducive to the accumulation of strain energy [24]. With the addition of RE elements, both $\{10\bar{1}1\}$ compression twins and $\{10\bar{1}1\}-\{10\bar{1}2\}$ secondary twins were activated and prevailed [24]. In case of compression and double twins, twinning aligns the basal planes favorably for basal slip, making the twinned regions undertake more plastic deformation compared to other regions [24]. Moreover, $\{10\bar{1}1\}$ and $\{10\bar{1}1\}-\{10\bar{1}2\}$ twins are not inclined to expand, thereby promoting the subdivision of grains [25].

TEM observations were taken at the central and periphery regions of the dicks after HPT processing. Fig.6a and 6b illustrate that a plenty of lamellas were observed at the center part of the 1/8-revolution disk. The selected area electron diffraction (SAED) patterns inserted in Fig.6a indicate that the lamellas A and B are $\{10\bar{1}1\}$ twins. Fig.6c and 6d show TEM images taken at the edge part of 1/8-revolution disk. Fig. 6c demonstrates that dislocation cell substructures were also developed. The diffraction spots extended in arc confirms the appearance of sub-grains with high internal strain.

As shown in Fig.6d, a number of lamella structures were also observed in this sample.

Fig.7 provides typical low-magnification TEM images of (a) the central region and (b) the edge region of the 5-revolution HPT disk, which corresponds to the region subjected to the largest plastic strain. Polycrystalline structure was observed in both (a) and (b), confirmed by the inserted SAED patterns. The average grain size in Fig.7b is around tens of nanometers, which is smaller than that in Fig.7a due to the larger plastic strain applied at the edge part of the disk. As shown in Fig.7c, it appears that some grains arrange along a line. It is proposed that these grains might be formed by subdivision of a twin via twin-twin or dislocation-twin interactions [26].

Fig. 8 shows the high-angle annular dark-field scanning transmission electron microscopy (HAADF-STEM) images and corresponding elemental mappings of areas containing precipitates taken at the central region of 5-revolution HPT sample. The contrast in HAADF image is uneven, which may be attributed to the local strain and the quite fine grain sizes caused by HPT deformation. The elemental mapping results indicate that the precipitates are rich in Gd and Zr, and the size of precipitates was in nanoscales, much smaller than that of the as-SSSS state shown in Fig. 1. In HPT processing, the local temperature rise brought by severe deformation may lead to dynamic recovery, which is unfavorable to grain refinement. However, Gd and Y elements tend to segregate to the grain boundaries and form precipitates, which benefit the dislocation entanglement and impede the dynamic recovery. Therefore alloying Mg with Gd and Y can not only help the formation of nanograins, but also improve the thermal stability of the alloy [27, 28].

As a material with hexagonal close packed (HCP) structure, there are not enough slip systems to satisfy the von Mises criterion in Mg alloy and the deformation twinning is critical for strain accommodation. The cooperation of multiple twinning modes may

benefit homogeneous deformation and allow HCP materials to deform to a large strain without failure [29]. Based on the detailed structure characterization in this study, it can be concluded that deformation induced multiple twinning played a crucial role in the microstructural evolution. The constrained HPT processing can effectively build up high local stresses to activate multiple twinning and suppress the crack propagation [30]. Therefore, the grain subdivision was achieved via twin-twin and dislocation-twin interactions. The activation of multiple twins contributes to the hardness increase in the 1/8-revolution HPT disk. The formation of nanocrystalline structure after 5-revolution HPT processing explains the highest hardness at the edge region of the 5-revolution disk. Note that the hardness reached ~120 Hv at the edge region of the 5-revolution disk, which is much higher than that achieved from traditional plastic deformation methods [31]. He et al. [31] reported that the microhardness was improved to ~90 Hv after extrusion at 350°C in an Mg-10Gd-2Y-0.5Zr alloy. A microhardness of ~100 Hv has been achieved in an Mg-14Gd-0.5Zr alloy processed by hot extrusion and hot rolling [32]. It is proposed that the much finer grain size achieved by HPT processing compared to other traditional deformation methods contributed to the higher hardness.

4. Conclusions

In this paper, the microstructural and hardness evolutions of an Mg-5.91Gd-3.29Y-0.54Zr (wt.%) alloy during HPT were investigated via optical microscope, electron back scattering diffraction, transmission electron microscope and Vicker hardness tests. Significant grain refinement was achieved in the HPT-processed Mg alloy as the number of revolutions increased to 5.

The results indicated that deformation twinning played a crucial role to accommodate the deformation process and to achieve significant grain refinement. At

low strains, primary twins were observed. With the increase of strain, the density of twins increased, and twins along different directions were activated and intersected. The activation of twins, together with the formation of dislocation cell substructures are the dominant mechanisms of the grain subdivision and subsequent hardness increase. Nanocrystalline structure was obtained after 5-revolution HPT processing, and the maximum hardness reached ~120 Hv, which is much higher than that achieved via conventional plastic deformation methods.

Credit authorship contribution statement

Xinyu Ren: Data Curation, Formal analysis, Writing - Original Draft, Review & Editing.

Xinglong An: Data Curation, Formal analysis.

Song Ni: Formal analysis, Writing - Review &Editing, Supervision.

Yi Huang: Data Curation, Writing - Review & Editing.

Min Song: Writing - Review & Editing.

Data Availability

All data used during the study are available from the corresponding author by request.

References

[1] S.R. Agnew, J.F. Nie, Preface to the viewpoint set on: The current state of magnesium alloy science and technology, Scripta Materialia 63(7) (2010) 671-673.

[2] Z. Yu, C. Xu, J. Meng, S. Kamado, Microstructure evolution and mechanical properties of a high strength Mg-11.7Gd-4.9Y-0.3Zr (wt%) alloy prepared by pre-deformation annealing, hot extrusion and ageing, Materials Science and Engineering: A 703 (2017) 348-358.

[3] F. Pan, M. Yang, X. Chen, A Review on Casting Magnesium Alloys: Modification of Commercial Alloys and Development of New Alloys, Journal of Materials Science & Technology 32(12) (2016) 1211-1221.

[4] J.-F. Nie, Precipitation and Hardening in Magnesium Alloys, Metallurgical and Materials Transactions A 43(11) (2012) 3891-3939.

[5] N. Stanford, D. Atwell, M.R. Barnett, The effect of Gd on the recrystallisation, texture and deformation behaviour of magnesium-based alloys, Acta Materialia 58(20) (2010) 6773-6783.

[6] L. Gao, R.S. Chen, E.H. Han, Effects of rare-earth elements Gd and Y on the solid solution strengthening of Mg alloys, Journal of Alloys and Compounds 481(1-2) (2009) 379-384.

[7] N. Stanford, The effect of rare earth elements on the behaviour of magnesium-based alloys: Part 2 – recrystallisation and texture development, Materials Science and Engineering: A 565 (2013) 469-475.

[8] E. Karakulak, A review: Past, present and future of grain refining of magnesium castings, Journal of Magnesium and Alloys 7(3) (2019) 355-369.

[9] Z. Zhang, J.-h. Zhang, J. Wang, Z.-h. Li, J.-s. Xie, S.-j. Liu, K. Guan, R.-z. Wu, Toward the development of Mg alloys with simultaneously improved strength and ductility by refining grain size via the deformation process, International Journal of Minerals, Metallurgy and Materials 28(1) (2020) 30-45.

[10] N. Tsuji, S. Ogata, H. Inui, I. Tanaka, J.P. Du, Strategy for managing both high strength and large ductility in structural materials–sequential nucleation of different deformation modes based on a concept of plaston, Scripta Materialia 181 (2020) 35-42.

[11] K. Wei, R. Hu, D. Yin, L. Xiao, S. Pang, Y. Cao, H. Zhou, Y. Zhao, Y. Zhu, Grain size effect on tensile properties and slip systems of pure magnesium, Acta Materialia 206 (2021).

[12] B. Wang, B. Tang, C. You, Y. Wan, Y. Gao, Z. Chen, L. Lu, C. Liu, J. Wang, Dislocation arrays, precipitate bands and free zones in forged Mg-Gd-Y-Zr alloy, Materials Science and Engineering: A 775 (2020).

[13] Z. Yang, C. Liu, Y. Gao, X. Guo, Y. Wan, Enhanced Mechanical and Corrosion Performance by Forming Micro Shear Bands in Cold Forged Mg-Gd-Y-Zr Alloy, Materials (Basel) 13(14) (2020).

[14] N. Stanford, M.R. Barnett, The origin of "rare earth" texture development in extruded Mg-based alloys and its effect on tensile ductility, Materials Science and Engineering: A 496(1-2) (2008) 399-408.

[15] J. Jiang, M. Song, H. Yan, C. Yang, S. Ni, Deformation induced dynamic recrystallization and precipitation strengthening in an MgZnMn alloy processed by high

strain rate rolling, Materials Characterization 121 (2016) 135-138.

[16] Z.-B. Chen, C.-M. Liu, H.-C. Xiao, J.-K. Wang, Z.-Y. Chen, S.-N. Jiang, Z.-J. Su, Effect of rolling passes on the microstructures and mechanical properties of Mg–Gd–Y–Zr alloy sheets, Materials Science and Engineering: A 618 (2014) 232-237.

[17] Y. Estrin, A. Vinogradov, Extreme grain refinement by severe plastic deformation: A wealth of challenging science, Acta Materialia 61(3) (2013) 782-817.

[18] R. Alizadeh, R. Mahmudi, P.H.R. Pereira, Y. Huang, T.G. Langdon, Microstructural evolution and superplasticity in an Mg–Gd–Y–Zr alloy after processing by different SPD techniques, Materials Science and Engineering: A 682 (2017) 577-585.

[19] R.B. Figueiredo, T.G. Langdon, Processing Magnesium and Its Alloys by High-Pressure Torsion: An Overview, Advanced Engineering Materials 21(1) (2019).

[20] S.V. Dobatkin, L.L. Rokhlin, E.A. Lukyanova, M.Y. Murashkin, T.V. Dobatkina, N.Y. Tabachkova, Structure and mechanical properties of the Mg-Y-Gd-Zr alloy after high pressure torsion, Materials Science and Engineering: A 667 (2016) 217-223.

[21] W.T. Sun, C. Xu, X.G. Qiao, M.Y. Zheng, S. Kamado, N. Gao, M.J. Starink, Evolution of microstructure and mechanical properties of an as-cast Mg-8.2Gd-3.8Y-1.0Zn-0.4Zr alloy processed by high pressure torsion, Materials Science and Engineering: A 700 (2017) 312-320.

[22] R.B. Figueiredo, S. Sabbaghianrad, A. Giwa, J.R. Greer, T.G. Langdon, Evidence for exceptional low temperature ductility in polycrystalline magnesium processed by severe plastic deformation, Acta Materialia 122 (2017) 322-331.

[23] Z.W. Huang, S.B. Jin, H. Zhou, Y.S. Li, Y. Cao, Y.T. Zhu, Evolution of twinning systems and variants during sequential twinning in cryo-rolled titanium, International Journal of Plasticity 112 (2019) 52-67.

[24] I. Basu, T. Al-Samman, Twin recrystallization mechanisms in magnesium-rare earth alloys, Acta Materialia 96 (2015) 111-132.

[25] D. Guan, W.M. Rainforth, J. Gao, J. Sharp, B. Wynne, L. Ma, Individual effect of recrystallisation nucleation sites on texture weakening in a magnesium alloy: Part 1-double twins, Acta Materialia 135 (2017) 14-24.

[26] Y. Gui, Y. Cui, H. Bian, Q. Li, L. Ouyang, A. Chiba, Role of slip and {10-12} twin on the crystal plasticity in Mg-RE alloy during deformation process at room temperature, Journal of Materials Science & Technology 80 (2021) 279-296.

[27] L.R. Xiao, X.F. Chen, Y. Cao, H. Zhou, X.L. Ma, D.D. Yin, B. Ye, X.D. Han, Y.T. Zhu, Solute segregation assisted nanocrystallization of a cold-rolled Mg–Ag alloy during annealing, Scripta Materialia 177 (2020) 69-73.

[28] L. Tang, Y. Zhao, R.K. Islamgaliev, R.Z. Valiev, Y.T. Zhu, Microstructure and thermal stability of nanocrystalline Mg-Gd-Y-Zr alloy processed by high pressure torsion, Journal of Alloys and Compounds 721 (2017) 577-585.

[29] Y. Cao, S. Ni, X. Liao, M. Song, Y. Zhu, Structural evolutions of metallic materials processed by severe plastic deformation, Materials Science and Engineering: R: Reports 133 (2018) 1-59.

[30] L. Tang, Y. Zhao, N. Liang, R.K. Islamgaliev, R.Z. Valiev, Y.T. Zhu, Localized deformation via multiple twinning in a Mg-Gd-Y-Zr alloy processed by high-pressure

torsion, Materials Science & Engineering A 677(nov.20) (2016) 68-75.

[31] S.M. He, X.Q. Zeng, L.M. Peng, X. Gao, J.F. Nie, W.J. Ding, Microstructure and strengthening mechanism of high strength Mg–10Gd–2Y–0.5Zr alloy, Journal of Alloys and Compounds 427(1-2) (2007) 316-323.

[32] R.G. Li, J.F. Nie, G.J. Huang, Y.C. Xin, Q. Liu, Development of high-strength magnesium alloys via combined processes of extrusion, rolling and ageing, Scripta Materialia 64(10) (2011) 950-953.
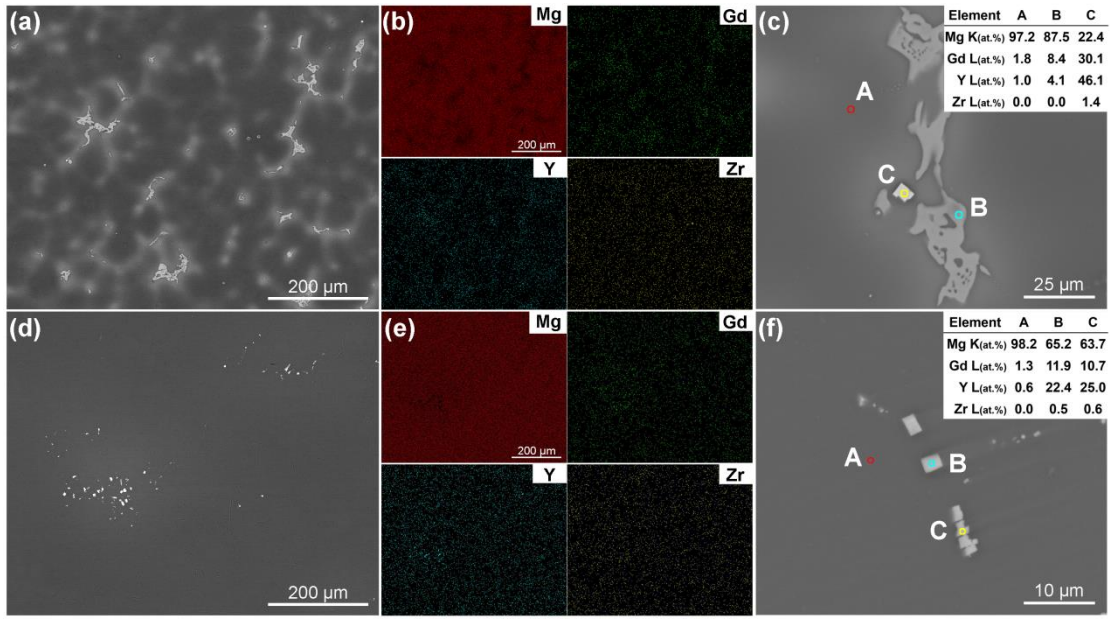
Fig. 1. The back-scattered SEM images, elemental mappings, EDS results of the

as-cast (a, b, c) and as-SSSS (d, e, f) samples
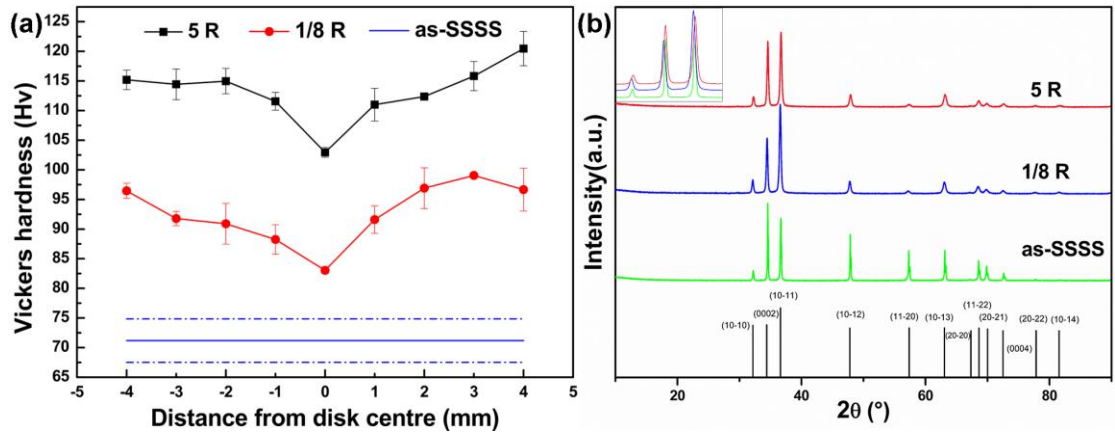
Fig. 2. (a) The distribution of microhardness and (b) XRD patterns of the as-SSSS

sample and 1/8-revolution and 5-revolution HPT disks
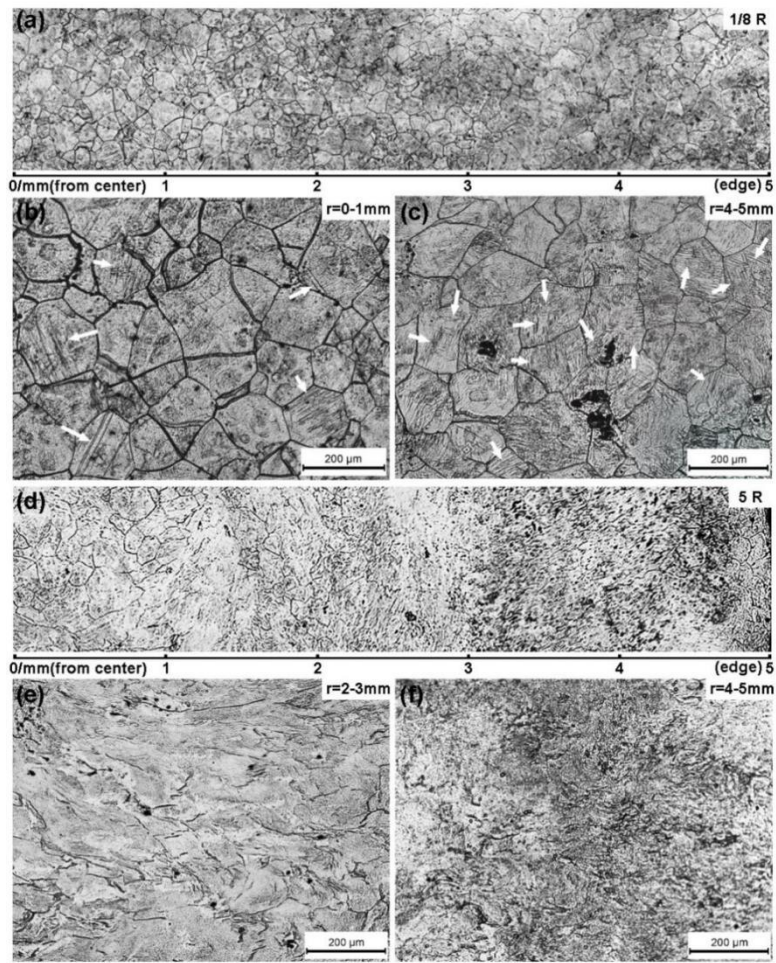
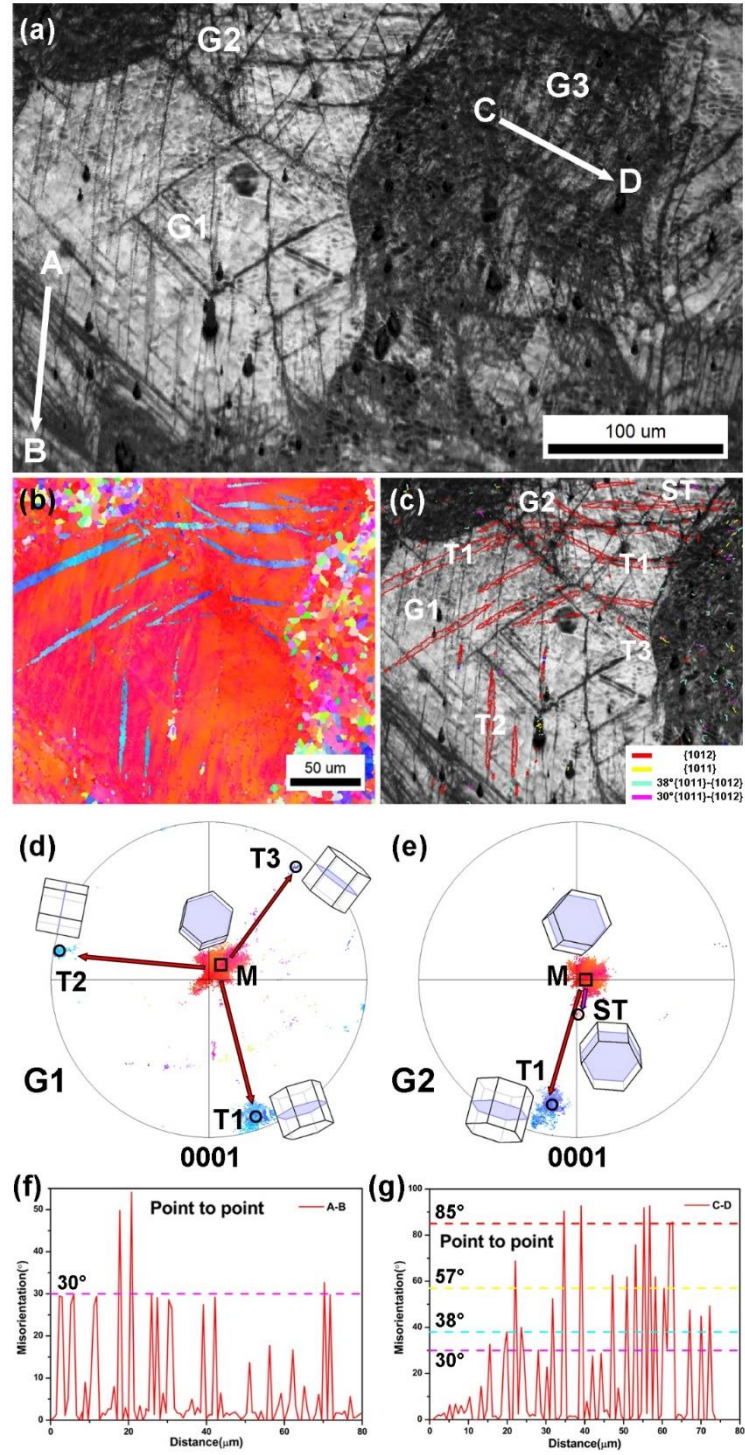Fig. 3. OM images across the radius of the (a, b, c) 1/8-revolution and (d, e, f) 5-revolution HPT processed disks.

Fig. 4. (a) Image quality figure of the center of 1/8-revolution disk, (b) inverse pole figure, (c) image quality figure, (d, e) pole figures of specific grains in (a), (f, g) line profiles of the misorientation angle along arrow AB in grain G1 and arrow CD in grain G3.
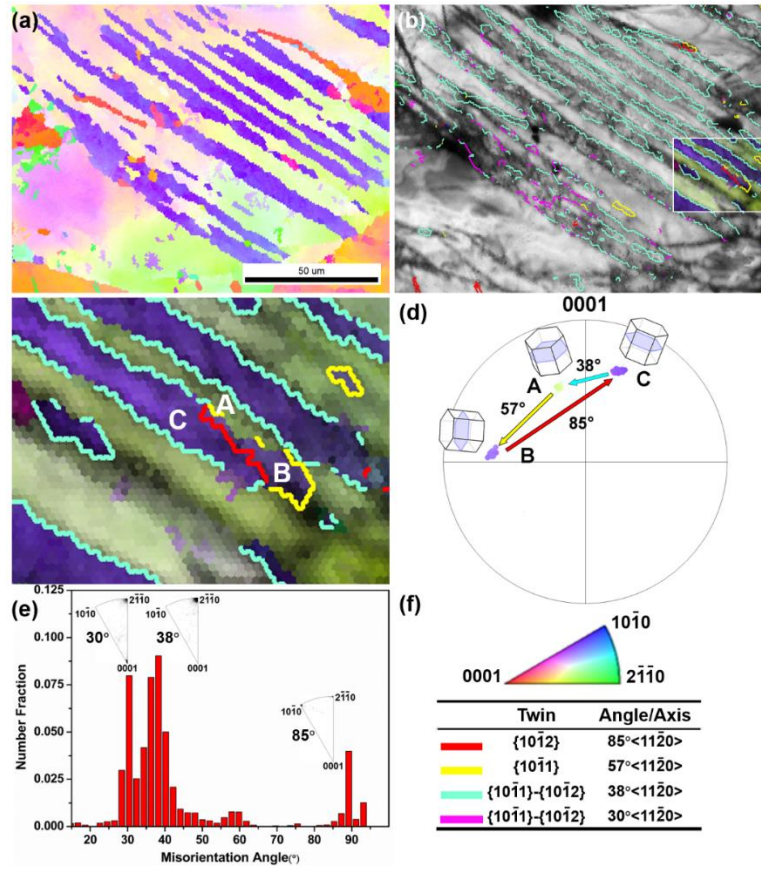
Fig. 5. (a) The inverse pole figure, (b) image quality figure, (c) the enlarged image of a rectangular area in (b), (d) corresponding pole figure in (c), (d) misorientation distribution figure, and (f) corresponding legend of the central area in the 1/8-revolution HPT processing disk.
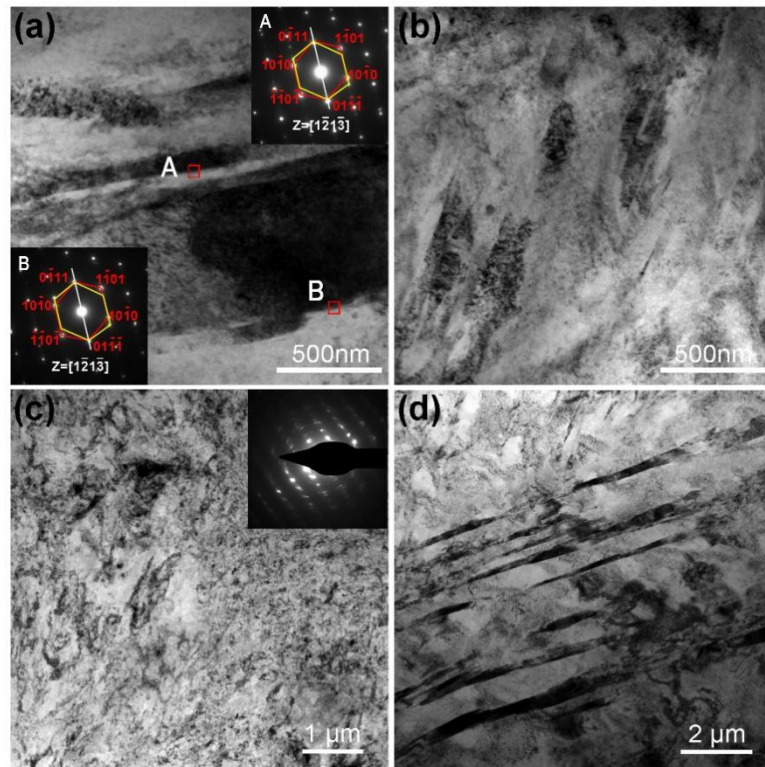
Fig. 6. TEM images taken from (a, b) the central and (c, d) the periphery regions

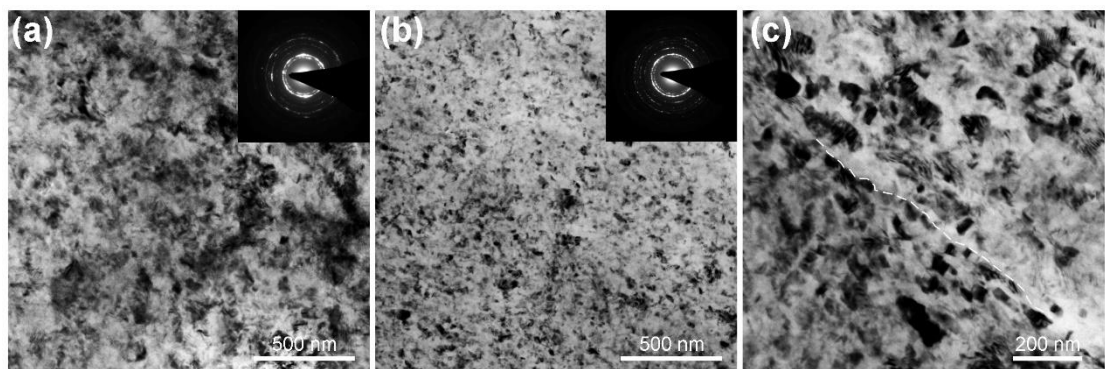of the disk after 1/8-revolution HPT processing.

Fig. 7. TEM images taken from (a) the central and (b, c) the periphery regions of

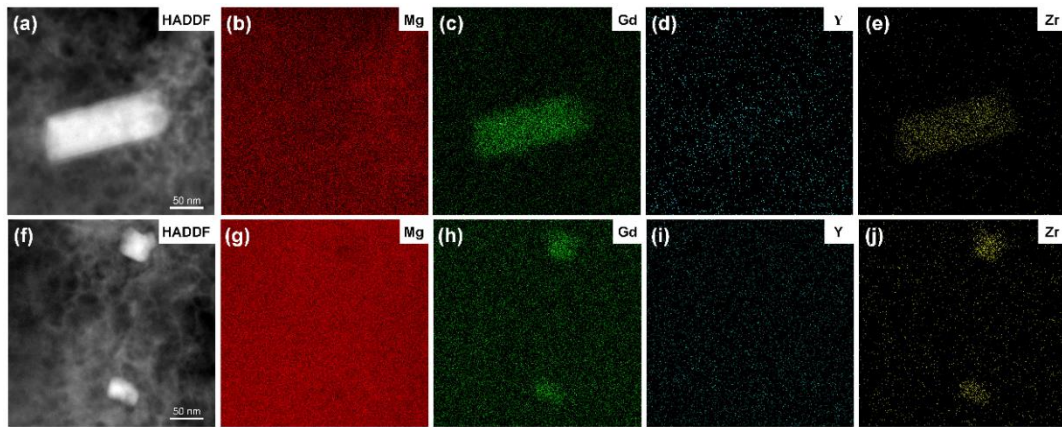the disk after 5-revolution HPT processing.

Fig. 8. HAADF-STEM images (a, f) and corresponding elemental mappings of (b, g) Mg, (c, h) Gd, (d, i) Y and (e, j) Zr at the central region of 5-revolution HPT sample.